GEOPHYSICS, VOL. 81, NO. 2 (MARCH-APRIL 2016); P. IM25–IM33, 12 FIGS.
10.1190/GEO2015-0381.1

Moving faults while unfaulting 3D seismic images

Xinming Wu[1], Simon Luo[2], and Dave Hale[1]

ABSTRACT

Unfaulting seismic images to correlate seismic reflectors across faults is helpful in seismic interpretation and is useful for seismic horizon extraction. Methods for unfaulting typically assume that fault geometries need not change during unfaulting. However, for seismic images containing multiple faults and, especially, intersecting faults, this assumption often results in unnecessary distortions in unfaulted images. We have developed two methods to compute vector shifts that simultaneously move fault blocks and the faults themselves to obtain an unfaulted image with minimal distortions. For both methods, we have used estimated fault positions and slip vectors to construct unfaulting equations for image samples alongside faults, and we have constructed simple partial differential equations for samples away from faults. We have solved these two different kinds of equations simultaneously to compute unfaulting vector shifts that are continuous everywhere except at faults. We have tested both methods on a synthetic seismic image containing normal, reverse, and intersecting faults. We also have applied one of the methods to a real 3D seismic image complicated by numerous intersecting faults.

INTRODUCTION

It is desirable to undo faulting in a seismic image to align seismic reflectors across faults. For example, from an unfaulted image with more continuous seismic reflectors, seismic horizons can be more easily interpreted. Automatic unfaulting of a seismic image often includes two steps: The first step is to estimate fault slip vectors for faults that are manually or automatically extracted from the seismic image. The second step is to extend estimated slip vectors away from samples on faults to all samples in the image and then simultaneously move fault blocks and even faults to obtain an unfaulted image.

For the first step, several methods have been proposed to estimate fault slip vectors that correlate seismic reflectors on opposite sides of precomputed faults. Fault slip estimated in this way is often dip slip, which is a vector, in the fault dip direction, representing displacement of the hanging-wall side of a fault surface relative to the footwall side. In a seismic image, fault strike slip is typically less apparent than dip slip, and it is therefore more difficult to estimate by correlating seismic reflectors. To correlate seismic reflectors on the opposite sides of a fault, Aurnhammer and Tonnies (2005) and Liang et al. (2010) propose windowed crosscorrelation methods; Hale (2013) uses a dynamic warping method that obviates correlation windows.

To simplify the second step, Wei and Maset (2005) and Wei (2009) assume that fault geometries need not change when unfaulting a seismic image. Luo and Hale (2013) also assume that fault positions are fixed during unfaulting. These assumptions make the unfaulting processing easier, but they might result in unnecessary distortions when unfaulting seismic images with multiple faults and, especially, intersecting faults. For example, in Figure 1, significant distortions are produced in the unfaulted image (Figure 1b) by fixing image samples adjacent to faults in the footwalls. Clearly, the faults, and especially fault A, must also be moved to obtain the unfaulted image with less distortion shown in Figure 1c.

In this paper, we first use the 3D image processing methods described by Wu and Hale (2015a) to automatically compute fault surfaces and dip slip vectors for image samples adjacent to faults. We then introduce two methods to compute unfaulting vector shifts for all samples in a seismic image by solving simple equations derived from the slip vectors. These computed vector shifts simultaneously move footwalls, hanging walls, and even the faults themselves, to undo faulting in a seismic image, with minimal distortion as shown in Figure 1c. As an additional test, we apply one of the two methods to a real 3D seismic image complicated by many intersecting faults. The unfaulted image with reflectors that are continuous across faults is then flattened using the unfolding method described by Luo and Hale (2013) to obtain a seismic horizon volume.

Manuscript received by the Editor 13 July 2015; revised manuscript received 9 November 2015; published online 15 March 2016.
[1]Colorado School of Mines, Golden, Colorado, USA. E-mail: xinwu@mines.edu; dhale@mines.edu.
[2]BP America Inc., Houston, Texas, USA. E-mail: sluosluo@gmail.com.

METHODS

Prior to unfaulting a 3D seismic image, we must first extract fault surfaces and estimate fault slip vectors. As shown in Figure 2, we use the method described by Wu and Hale (2015a) to automatically compute fault surfaces (Figure 2b) and fault dip slips, the components of fault slips in the fault dip directions (Figure 2b). Fault dip slip is a vector, and the vertical component of this vector is fault throw, which is represented by colors on the fault surfaces in Figure 2b. The horizontal components of slip vectors in the inline and crossline directions are not shown in this paper. Fault throw can also be displayed as a 3D image (with mostly null values) overlaid with the seismic image in Figure 2c. Note that fault throws are nonnegative for faults A, C, and D, but they are negative for fault B, which indicates that faults A, C, and D are normal faults, whereas fault B is a reverse fault. For the intersecting faults A and D, the older fault A is dislocated by the younger fault D. Therefore, to undo the faulting for faults A and D, we must move the faults as well as the adjacent fault blocks.

As shown in Figure 2c, fault slips are estimated only at the locations of faults. However, to undo faulting apparent in a seismic image without distorting the image, we cannot shift only the image samples adjacent to faults. Instead, we must shift all samples in the image and move entire fault blocks and even the faults themselves. Wei and Maset (2005) and Luo and Hale (2013) propose to extend fault slips away from faults into fault blocks to compute unfaulting shifts that only move fault blocks but fix fault locations. Without shifting faults, however, these methods cannot correctly undo faulting in an image containing complicated faults, especially intersecting faults, like those shown in Figure 2.

We propose two methods to compute vector shifts for all samples in an image, by solving simple equations derived from fault slips on faults, to move faults and fault blocks simultaneously.

Mappings between input and unfaulted spaces

Let $f(\mathbf{x})$ denote an input 3D seismic image, a sampled function of coordinates $\mathbf{x} \equiv (x_1, x_2, x_3)$ in the input space. To undo faulting in

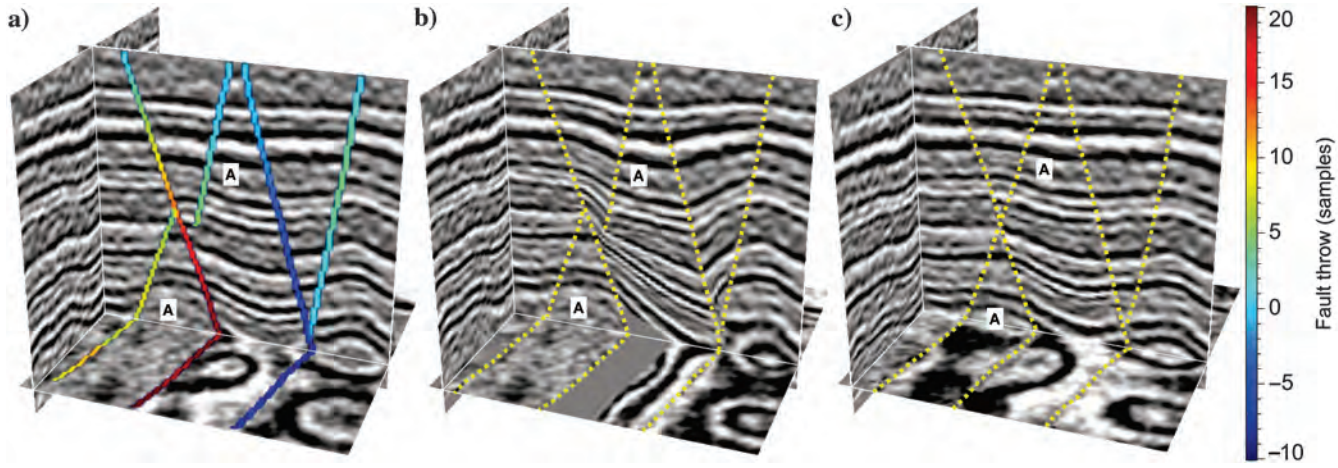

Figure 1. (a) A 3D synthetic seismic image with faults colored by fault throws is significantly distorted when (b) unfaulted by moving only fault blocks while fixing fault positions. (c) Faults (especially fault A) must also be moved to obtain an unfaulted image with minimal distortions.

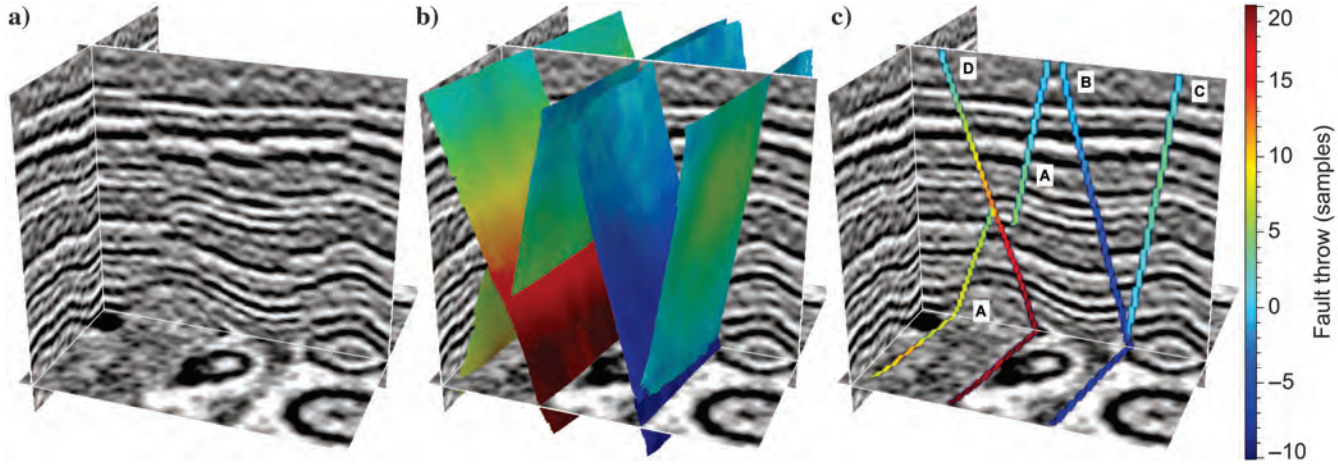

Figure 2. (a) Given a 3D seismic image, we extract (b) fault surfaces and estimate fault dip slip vectors for each sample on fault surfaces. Faults in panels (b and c) are colored by fault throws, the vertical components of slip vectors.

this image, we must find a mapping $\mathbf{x}(\mathbf{w})$, where $\mathbf{w} \equiv (w_1, w_2, w_3)$ are coordinates in the unfaulted (output) space, and then compute an unfaulted image

$$h(\mathbf{w}) = f[\mathbf{x}(\mathbf{w})]. \tag{1}$$

We express the mapping $\mathbf{x}(\mathbf{w})$ in terms of a shift vector field $\mathbf{r}(\mathbf{w})$ defined in the unfaulted space:

$$\mathbf{x}(\mathbf{w}) = \mathbf{w} + \mathbf{r}(\mathbf{w}). \tag{2}$$

Therefore, the desired mapping $\mathbf{x}(\mathbf{w})$ can be obtained by solving for the shift vector field $\mathbf{r}(\mathbf{w})$. For any location $\mathbf{w}$ in the sampling grid of the unfaulted space, this mapping $\mathbf{x}(\mathbf{w})$ tells us where to find the corresponding sample in the input space. However, it can be difficult to directly solve for the shift vector field $\mathbf{r}(\mathbf{w})$ in the unfaulted space because fault locations and slip vectors are computed in the input space.

We assume that the mapping $\mathbf{x}(\mathbf{w})$ from unfaulted coordinates $\mathbf{w}$ to input coordinates $\mathbf{x}$ is reversible. This means that we can find a mapping $\mathbf{w}(\mathbf{x})$ that converts points from the input space to the unfaulted space. We express $\mathbf{w}(\mathbf{x})$ in terms of a shift vector field $\mathbf{s}(\mathbf{x})$ in the input space:

$$\mathbf{w}(\mathbf{x}) = \mathbf{x} - \mathbf{s}(\mathbf{x}). \tag{3}$$

We can usually find this shift vector field $\mathbf{s}(\mathbf{x})$ in the input space by using the fault locations and dips that we have in the input space, and we thereby obtain the mapping $\mathbf{w}(\mathbf{x})$. However, if applied directly to a uniformly sampled input image $f(\mathbf{x})$, the mapping $\mathbf{w}(\mathbf{x})$ yields an irregularly sampled unfaulted image $h(\mathbf{w}(\mathbf{x})) = f(\mathbf{x})$. Therefore, we instead use inverse mapping $\mathbf{x}(\mathbf{w})$ and 3D sinc interpolation of $f(\mathbf{x})$ to compute a uniformly sampled image $h(\mathbf{w}) = f(\mathbf{x}(\mathbf{w}))$.

For these reasons, we first solve for the shift vector field $\mathbf{s}(\mathbf{x})$ in the input space, and we then convert $\mathbf{s}(\mathbf{x})$ to the shift vector field $\mathbf{r}(\mathbf{w})$ in the unfaulted space, which is then used to compute the mapping $\mathbf{x}(\mathbf{w}) = \mathbf{w} + \mathbf{r}(\mathbf{w})$ and the unfaulted image $h(\mathbf{w})$.

Assuming that the mapping between the input and unfaulted spaces is reversible, equations 2 and 3 imply the following relationship between the shift vector fields $\mathbf{s}(\mathbf{x})$ and $\mathbf{r}(\mathbf{w})$:

$$\mathbf{r}(\mathbf{w}(\mathbf{x})) = \mathbf{s}(\mathbf{x}). \tag{4}$$

We solve this equation for $\mathbf{r}(\mathbf{w})$ using an iterative method. We begin with an initial shift vector field $\mathbf{r}_0(\mathbf{w}) = \mathbf{s}(\mathbf{w})$, and then iteratively update the initial shift vector field to compute $\mathbf{r}(\mathbf{w})$:

$$\begin{aligned}
\mathbf{r}_0(\mathbf{w}) &= \mathbf{s}(\mathbf{w}),\\
\mathbf{x}_0(\mathbf{w}) &= \mathbf{w} + \mathbf{r}_0(\mathbf{w}),\\
\mathbf{r}_1(\mathbf{w}) &= \mathbf{s}(\mathbf{x}_0(\mathbf{w})),\\
\mathbf{x}_1(\mathbf{w}) &= \mathbf{w} + \mathbf{r}_1(\mathbf{w}),\\
&\cdots\\
\mathbf{r}_i(\mathbf{w}) &= \mathbf{s}(\mathbf{x}_{i-1}(\mathbf{w})),\\
\mathbf{x}_i(\mathbf{w}) &= \mathbf{w} + \mathbf{r}_i(\mathbf{w}),\\
&\cdots\\
\mathbf{r}(\mathbf{w}) \approx \mathbf{r}_m(\mathbf{w}) &= \mathbf{s}(\mathbf{w} + \mathbf{r}_{m-1}(\mathbf{w})).
\end{aligned} \tag{5}$$

In this way, we update the shift vector field $\mathbf{r}_i(\mathbf{w})$, until the updates are insignificant in the mth iteration, to obtain the shift vector field $\mathbf{r}(\mathbf{w}) \approx \mathbf{r}_m(\mathbf{w})$ in the unfaulted space. This iterative process is fast because only a nearest neighbor interpolation method is needed when computing $\mathbf{r}_i(\mathbf{w}) = \mathbf{s}(\mathbf{w} + \mathbf{r}_{i-1}(\mathbf{w}))$. In practice, we find that $m = 20$ iterations are sufficient. Therefore, we can efficiently compute $\mathbf{r}(\mathbf{w})$ in the unfaulted space if we already know $\mathbf{s}(\mathbf{x})$ in the input space.

To compute the shift vector field $\mathbf{s}(\mathbf{x})$ in the input space, we propose two methods that solve simple equations derived from slip vectors estimated at faults.

Vector shifts in input space

As discussed by Rice (1983), faults can be considered as surfaces of slip (displacement) discontinuity in surroundings with continuous slip. This means that when a fault is formed, the slip vector field generating this fault should be continuous in neighboring fault blocks but is discontinuous at the fault. Therefore, to undo faulting apparent in a seismic image, we must compute unfaulting shifts that are also continuous in fault blocks and discontinuous at faults. Accordingly, we define equations of unfaulting differently for image samples alongside faults and for those elsewhere within fault blocks.

After estimating fault slips shown in Figures 2b and 2c, we are able to compute unfaulting shifts for the samples adjacent to faults. Figure 3 shows an example of a slip vector $\mathbf{t}(\mathbf{x}_a)$ estimated at a sample $\mathbf{x}_a$ adjacent to a fault from footwall; this slip vector indicates how to correlate the image sample at $\mathbf{x}_a$ in the footwall to the corresponding sample at $\mathbf{x}_b = \mathbf{x}_a + \mathbf{t}(\mathbf{x}_a)$ in the hanging wall. Image samples $\mathbf{x}_a$ and $\mathbf{x}_b$ must be located at the same position in the unfaulted space:

$$\mathbf{w}(\mathbf{x}_a) = \mathbf{w}(\mathbf{x}_b), \tag{6}$$

which can be rewritten using equation 3 as

$$\mathbf{x}_a - \mathbf{s}(\mathbf{x}_a) = \mathbf{x}_b - \mathbf{s}(\mathbf{x}_b). \tag{7}$$

Because $\mathbf{x}_b = \mathbf{x}_a + \mathbf{t}(\mathbf{x}_a)$, we have

$$\mathbf{s}(\mathbf{x}_b) - \mathbf{s}(\mathbf{x}_a) = \mathbf{t}(\mathbf{x}_a). \tag{8}$$

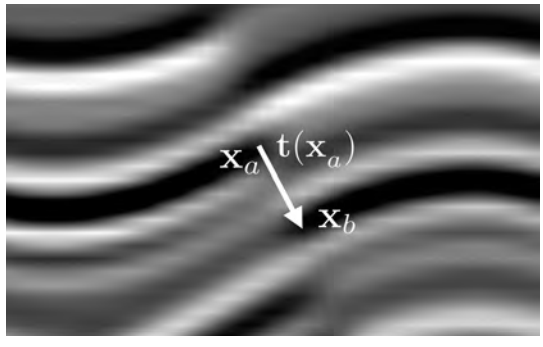

Figure 3. A fault slip vector $\mathbf{t}(\mathbf{x}_a)$, estimated at each footwall sample adjacent to a fault, tells us how to correlate the image sample at $\mathbf{x}_a$ in the footwall to the corresponding sample $\mathbf{x}_b$ in the hanging wall.

Because the shifts $\mathbf{s}$ and slips $\mathbf{t}$ are vectors, equation 8 represents three equations, one for each component, and we can write the three equations as

$$s_k(\mathbf{x}_b) - s_k(\mathbf{x}_a) = t_k(\mathbf{x}_a), \tag{9}$$

where $k = 1$, 2 and 3 are indices representing the components of vectors in the crossline, inline, and vertical directions, respectively.

Recall that we estimate slip vectors everywhere within faults, which means that we have unfaulting equation 9 for all image samples alongside faults. Assuming that slip vectors are estimated for L samples on faults, then we have L unfaulting equations for each component of our desired vector shifts.

Equation 9 applies only to those samples alongside faults. For other samples away from faults, we expect unfaulting shifts to vary slowly and continuously. Thus, derivatives of each component of the vector shift $\mathbf{s}(\mathbf{x})$ should be nearly zero:

$$\omega(\mathbf{x})\nabla s_k(\mathbf{x}) \approx \mathbf{0}, \tag{10}$$

where ∇ represents the gradient operator and $s_k(\mathbf{x})(k = 1, 2, 3)$ represent the three components of vector shifts for all samples in an image. Here, $\omega(\mathbf{x})$ is a weighting function that is zero at image samples adjacent to faults, and it is one elsewhere. Therefore, equation 10 is used for all image samples except those adjacent to faults.

Having defined unfaulting equation 9 for image samples alongside faults and the smoothing equation 10 for samples elsewhere, we can now solve for the unfaulting shifts $\mathbf{s}(\mathbf{x})$. We propose two methods to simultaneously solve these unfaulting and smoothing equations for $\mathbf{s}(\mathbf{x})$ in two different ways. Both methods work well for the examples in this paper, but they are derived based on different assumptions about the estimated slip vectors, and they use the unfaulting equation 9 in different ways. Method 1 assumes that slip vectors are estimated for most samples on faults, but that the estimated slips might be inaccurate for some samples. Method 2 assumes that slip vectors are picked manually for a limited number of samples on faults, and that these slip vectors are accurate.

Method 1

In practice, automatically estimated slip vectors might be inaccurate for some samples on faults. In such a situation, we want to rewrite equation 9 as an approximation:

$$s_k(\mathbf{x}_b) - s_k(\mathbf{x}_a) \approx t_k(\mathbf{x}_a). \tag{11}$$

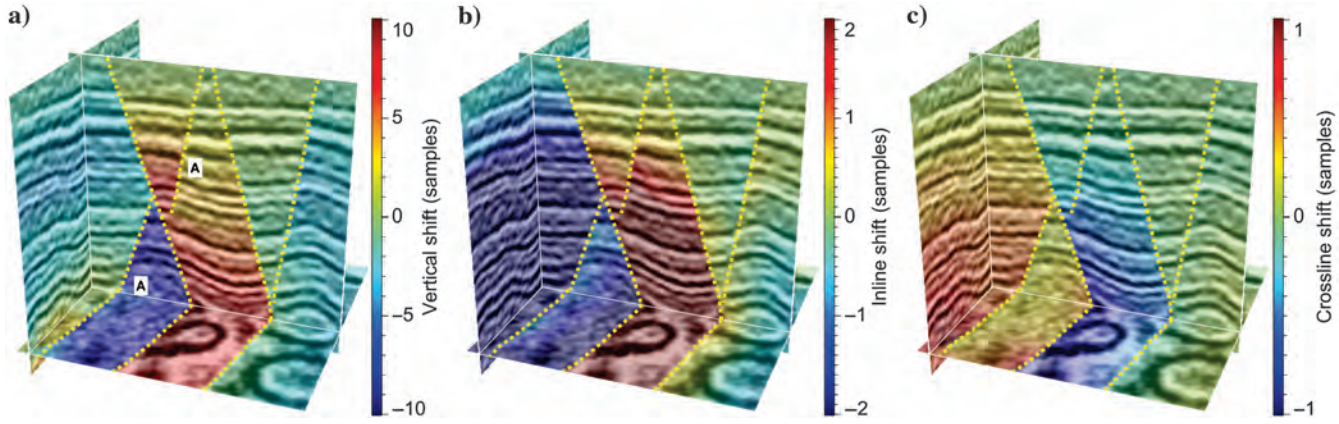

Figure 4. (a) Vertical, (b) inline, and (c) crossline components of unfaulting shifts $\mathbf{s}(\mathbf{x})$ are computed in the input space using method 1. Discontinuities in each component of shifts coincide with fault locations.

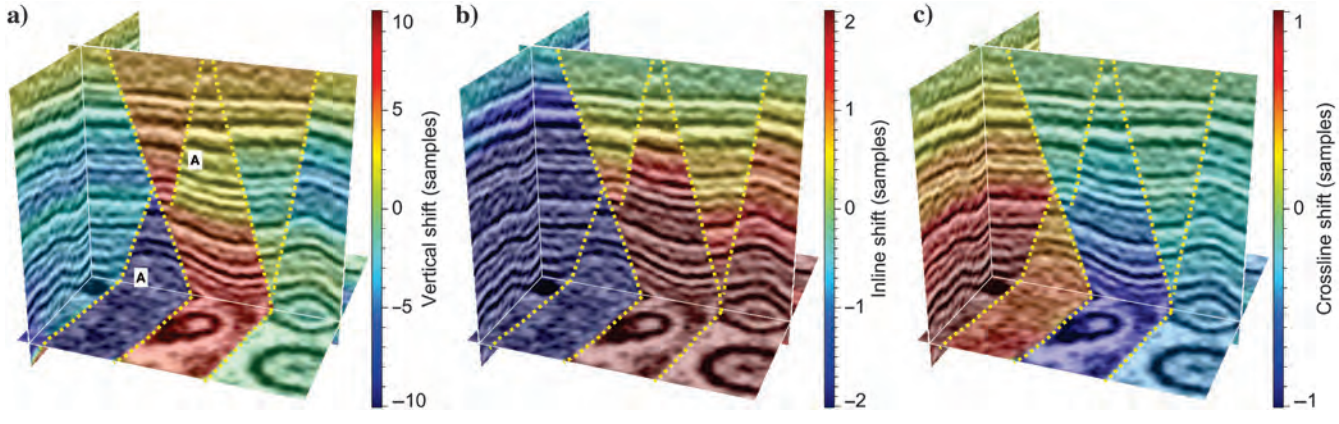

Figure 5. (a) Vertical, (b) inline, and (c) crossline components of unfaulting shifts $\mathbf{s}(\mathbf{x})$ are computed in the input space using method 2. Discontinuities in each component of shifts coincide with fault locations.

In addition, if we have a measure $c(\mathbf{x})$ of the quality of the estimated slip vectors at faults, we can use this measure to weight equation 11 so that samples with well estimated slips are weighted more than those with poorly estimated slips:

$$c(\mathbf{x}_a)(s_k(\mathbf{x}_b) - s_k(\mathbf{x}_a)) \approx c(\mathbf{x}_a)t_k(\mathbf{x}_a). \quad (12)$$

For the examples in this paper, the measure $c(\mathbf{x})$ is fault likelihood (Wu and Hale, 2015a), which we compute for every

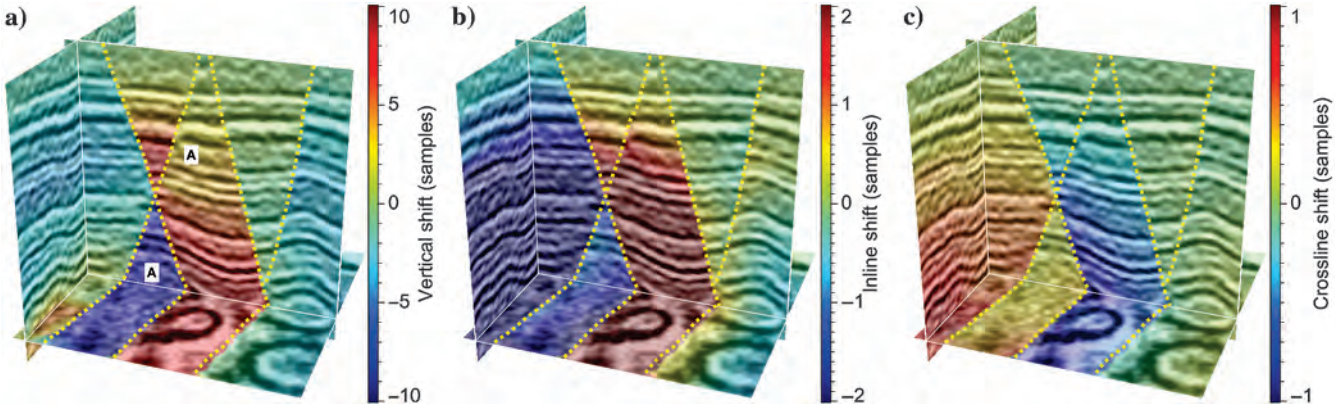

Figure 6. (a) Vertical, (b) inline, and (c) crossline components of unfaulting shifts in the unfaulted space are converted from those in the input space shown in Figure 4. The discontinuities on each component of shifts are displaced relative to those in Figure 4.

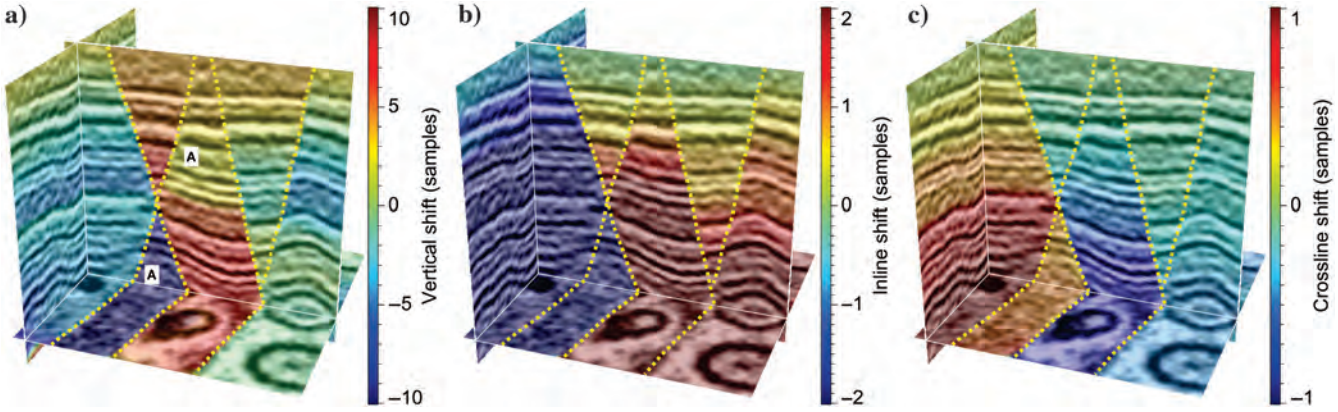

Figure 7. (a) Vertical, (b) inline, and (c) crossline components of unfaulting shifts in the unfaulted space are converted from those in the input space shown in Figure 5. The discontinuities on each component of shifts are displaced relative to those in Figure 5.

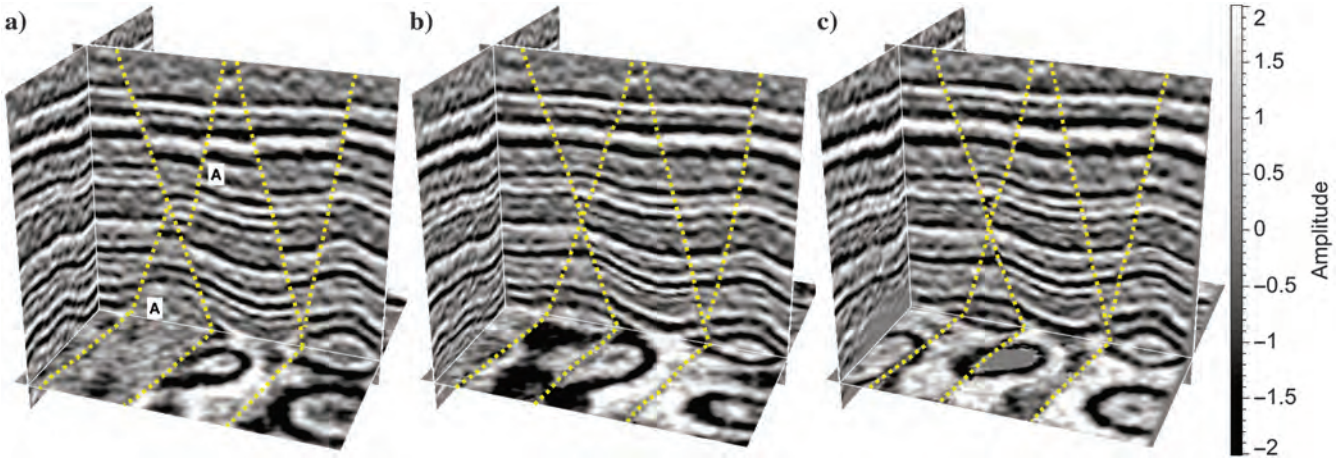

Figure 8. (a) The input synthetic seismic image is (b) unfaulted using shifts in Figure 6 computed by method 1, and (c) using shifts in Figure 7 computed by method 2.

image sample location $\mathbf{x}$, where the slip vector $\mathbf{t}(\mathbf{x})$ is also estimated.

To compute unfaulting shifts for all samples in an image, we solve equations 10 and 12 simultaneously:

$$\begin{aligned} \omega(\mathbf{x})\nabla s_k(\mathbf{x}) &\approx \mathbf{0}, \\ \beta c(\mathbf{x}_a)(s_k(\mathbf{x}_b) - s_k(\mathbf{x}_a)) &\approx \beta c(\mathbf{x}_a) t_k(\mathbf{x}_a), \end{aligned} \tag{13}$$

where we have introduced the parameter β to balance the two equations. For all examples in this paper, we use $\beta = N/L$, where L is the number of samples on faults and N is the number of all samples in a seismic image. Although we solve the two equations simultaneously, the second equation is defined only for samples adjacent to faults, where the first equation is disabled because $\omega(\mathbf{x})$ is zero for those samples.

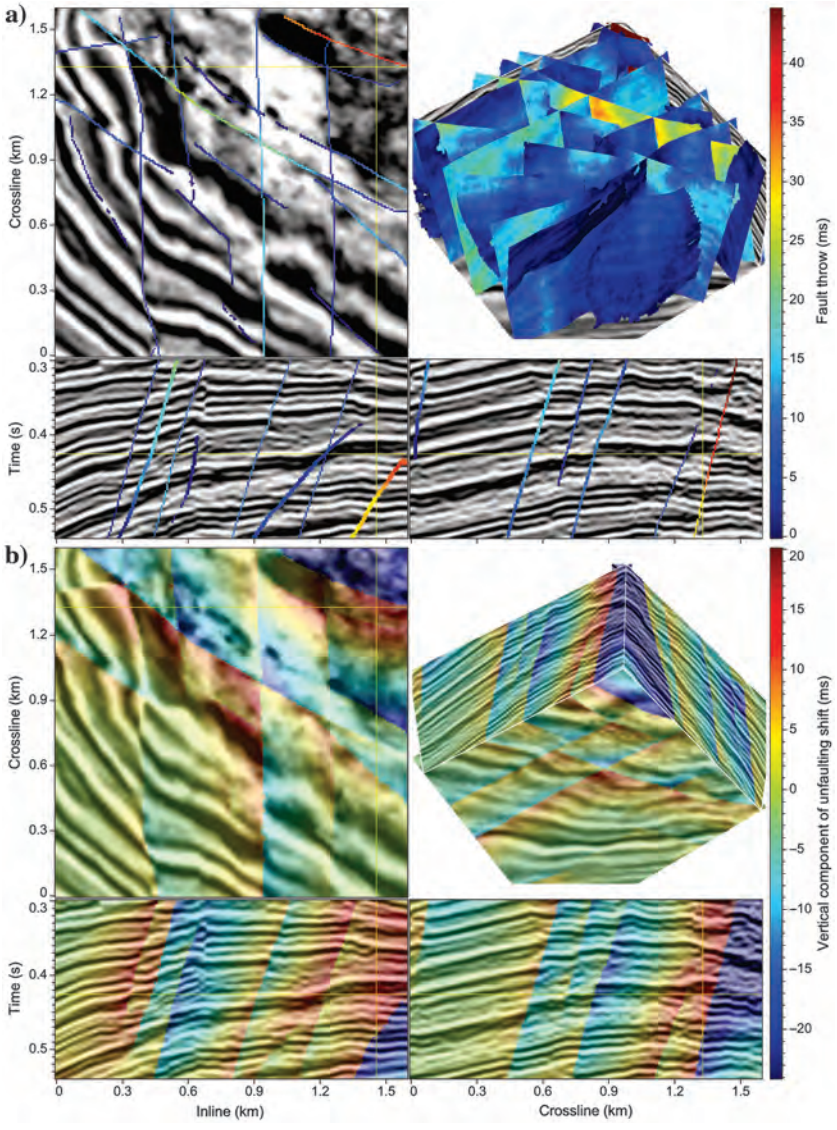

Figure 9. (a) Fault surfaces and slip vectors are first estimated from a 3D seismic image, and they then are used to compute (b) unfaulting vector shifts used in image unfaulting. Only vertical components of vectors are shown here.

Because equations 13 for the different components ($k = 1, 2, 3$) of vector shifts are not coupled with each other, we can solve for each component independently. We use the vertical component ($k = 3$) to explain how to solve these equations:

$$\begin{aligned} \omega(\mathbf{x})\nabla s_3(\mathbf{x}) &\approx \mathbf{0}, \\ \beta c(\mathbf{x}_a)(s_3(\mathbf{x}_b) - s_3(\mathbf{x}_a)) &\approx \beta c(\mathbf{x}_a) t_3(\mathbf{x}_a). \end{aligned} \tag{14}$$

These equations can be represented in matrix-vector form as

$$\begin{bmatrix} \mathbf{WG} \\ \mathbf{CM} \end{bmatrix} \mathbf{s} \approx \begin{bmatrix} \mathbf{0} \\ \mathbf{Ct} \end{bmatrix}, \tag{15}$$

where $\mathbf{s}$ is a $N \times 1$ vector representing the unknown vertical shifts for a 3D image with N samples; $\mathbf{G}$ is a $3N \times N$ matrix representing finite-difference approximations of the gradient operator; $\mathbf{W}$ is a $3N \times 3N$ diagonal matrix with zeros and ones on the diagonal entries, the zeros corresponding to samples adjacent to faults, and the ones corresponding to samples away from faults; $\mathbf{t}$ is an $L \times 1$ vector containing the vertical component of slip vectors estimated for L ($L < N$) samples on faults; $\mathbf{C}$ is an $L \times L$ diagonal matrix with fault likelihoods scaled by β on the diagonal; and $\mathbf{M}$ is an $L \times N$ sparse matrix with mostly zeros, ones for the samples adjacent to faults in hanging walls, and negative ones for the samples adjacent to faults in footwalls.

In total, we have $3N + L$ equations for only N unknowns. Therefore, we might compute a least-squares solution of equation 15 by solving the normal equations:

$$\mathbf{G}^\top\mathbf{W}^\top\mathbf{WGs} + \mathbf{M}^\top\mathbf{C}^\top\mathbf{CMs} = \mathbf{M}^\top\mathbf{C}^\top\mathbf{Ct}, \tag{16}$$

where the first term corresponds to the smoothing equation 10. In practice, however, fault dip slips typically vary mainly in dip directions, which are often more consistent in directions normal to seismic reflectors than in directions parallel to those reflectors. Therefore, instead of the isotropic smoothing used in equation 16, we should smooth less for unfaulting shifts in directions normal to reflectors than in directions parallel to reflectors.

To implement this anisotropic smoothing of unfaulting shifts, we modify the first term in equation 16 by adding a matrix $\mathbf{D}$:

$$\mathbf{G}^\top\mathbf{W}^\top\mathbf{DWGs} + \mathbf{M}^\top\mathbf{C}^\top\mathbf{CMs} = \mathbf{M}^\top\mathbf{C}^\top\mathbf{Ct}. \tag{17}$$

The matrix $\mathbf{D}$ contains spatially varying tensors derived from structure tensors (Van Vliet and Verbeek, 1995; Fehmers and Höcker, 2003) computed for all image samples. Each tensor $\mathbf{T}$ represented in the matrix $\mathbf{D}$ is a 3×3 symmetric positive-definite matrix with eigen decomposition

$$\mathbf{T} = \lambda_1 \mathbf{v}_1 \mathbf{v}_1^\top + \lambda_2 \mathbf{v}_2 \mathbf{v}_2^\top + \lambda_3 \mathbf{v}_3 \mathbf{v}_3^\top, \tag{18}$$

where $\mathbf{v}_1$ is an eigenvector normal to seismic reflectors and $\mathbf{v}_2$ and $\mathbf{v}_3$ are eigenvectors that lie within a plane tangent to seismic reflectors. Eigenvalues λ_1, λ_2, and λ_3, all in the range $[0,1]$, correspond to eigenvectors $\mathbf{v}_1$, $\mathbf{v}_2$, and $\mathbf{v}_3$, respectively. For the examples in this paper, we set $\lambda_1 = 0.01$, $\lambda_2 = \lambda_3 = 1.0$ to construct the tensor matrix $\mathbf{D}$, so that unfaulting shifts are smoothed in directions normal to reflectors less than in directions parallel to reflectors.

Note that to solve equation 17 for the vertical shifts $\mathbf{s}$, we do not explicitly form the matrices in this equation. The matrices $\mathbf{G}^\top\mathbf{W}^\top\mathbf{DWG}$ and $\mathbf{M}^\top\mathbf{C}^\top\mathbf{CM}$ on the left side are symmetric positive definite; therefore, we can solve the equation using a conjugate gradient (CG) method, which requires only the computation of matrix-vector products in this equation. Similarly, we can also solve for the horizontal components of the unfaulting vector shifts in inline and crossline directions.

For example, we use slip vectors, estimated on the fault surfaces shown in Figure 2, to construct the coefficients in equation 17. Then, solving this equation, we compute the vertical, inline, and crossline components of the unfaulting shifts shown in Figure 4a, 4b, and 4c, respectively. We observe that the shifts are discontinuous at faults and continuous elsewhere, as expected.

Method 2

For method 1, we assumed that fault slip vectors are estimated using an automatic method for most samples on faults, and, as a result, they might be inaccurate for some samples. However, in an interactive interpretation system, one might manually pick pairs of points, for example, $\mathbf{x}_a$ and $\mathbf{x}_b$ in Figure 3, alongside a fault, and then simply compute corresponding slip vectors $\mathbf{t}(\mathbf{x}_a) = \mathbf{x}_b - \mathbf{x}_a$.

In this case, we expect the unfaulting equation 9 with interpreted slip vectors to be strictly satisfied for manually picked pairs of points alongside a fault. At the same time, however, we still expect shifts to vary smoothly within fault blocks, for all image samples located away from faults. Therefore, for method 2, instead of solving equation 17, we compute the unfaulting shifts by solving

$$\mathbf{G}^\top\mathbf{W}^\top\mathbf{DWGs} = \mathbf{0} \quad \text{subject to } \mathbf{Ms} = \mathbf{t}. \tag{19}$$

As discussed by Wu and Hale (2015b), we use a preconditioned CG method to solve this linear system with hard constraints. The unfaulting equation $\mathbf{Ms} = \mathbf{t}$ is implemented with simple preconditioners in the CG method; the details of constructing such preconditioners are discussed by Wu and Hale (2015b). Starting with initial shifts that satisfy the unfaulting equation $\mathbf{Ms} = \mathbf{t}$, the CG iterates update the shifts for all samples, whereas the preconditioners guarantee that the updated shifts always satisfy the unfaulting equation after each iteration.

To test this method, we used our automatically estimated fault slips to construct the unfaulting equation $\mathbf{Ms} = \mathbf{t}$ for all samples alongside faults, and compute initial shifts with which the CG method begins. The computed vertical, inline, and crossline components of vector shifts are shown in Figure 5a, 5b, and 5c, respectively. Similar to the shifts computed using method 1, each component of shifts computed using this method is discontinuous at faults and smoothly varying elsewhere.

Vector shifts in the unfaulted space

The shifts $\mathbf{s}(\mathbf{x})$ computed by the two methods above all are in the input space. We must map them into the unfaulted space before unfaulting the seismic image. We obtain the corresponding vector

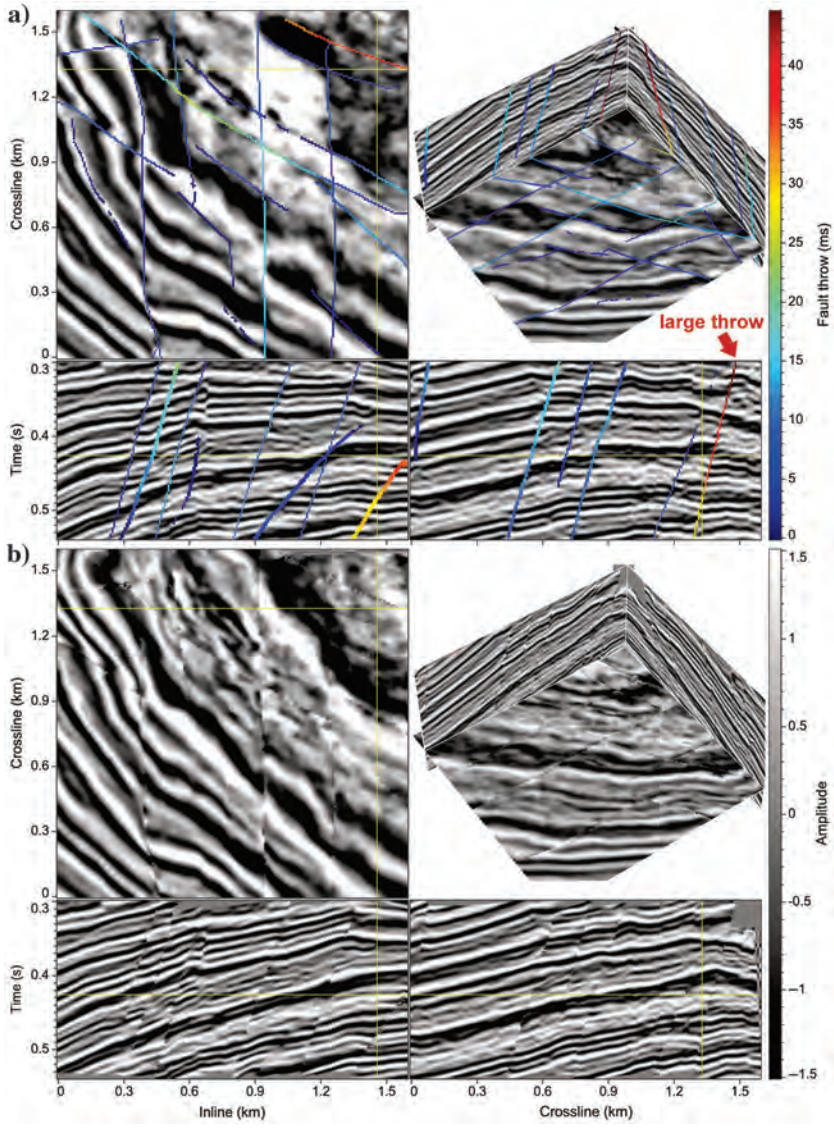

Figure 10. A 3D seismic image (a) before and (b) after unfaulting. In all image slices, seismic reflectors are more continuous after unfaulting. For the large-throw fault highlighted by a red arrow in panel (a), the corresponding fault blocks are significantly moved in panel (b) to align the seismic reflectors on opposite sides of this fault.

shifts $\mathbf{r}(\mathbf{w})$ in the unfaulted space using the efficient iteration method in equation 5.

Figure 6 shows all components of vector shifts $\mathbf{r}(\mathbf{w})$ obtained in this way from the vector shifts $\mathbf{s}(\mathbf{x})$ (Figure 4) computed in the input space using method 1. Figure 7 shows all components of vector shifts $\mathbf{r}(\mathbf{w})$ converted from the vector shifts $\mathbf{s}(\mathbf{x})$ (Figure 5) computed in the input space using method 2. Before conversion, we observe that discontinuities in each component of shifts coincide with faults in the input space, as in Figures 4 and 5. However, after converting shifts to the unfaulted space, the discontinuities on each component of shifts in Figures 6 and 7 are displaced relative to those in Figures 4 and 5.

Using the converted vector shifts $\mathbf{r}(\mathbf{w})$ in Figures 6 (method 1) and 7 (method 2), we obtain the corresponding unfaulting mapping $\mathbf{x}(\mathbf{w}) = \mathbf{w} + \mathbf{r}(\mathbf{w})$, and then compute the unfaulted images as shown in Figure 8b (method 1) and 8c (method 2). In both unfaulted images, seismic reflectors are more continuous than those in the input seismic image (Figure 8a). We also observe that the faults are shifted in the unfaulted space, relative to the input space. For example, fault A is dislocated in the original seismic image (Figure 8a) by its intersecting fault, but it is relocated in both unfaulted images (Figure 8b and 8c) computed using two different methods.

As shown in Figure 8b and 8c, both methods provide unfaulted images with minimal distortions because slip vectors (Figure 2) are estimated accurately for all faults in this synthetic example. In practice, however, we suggest using method 1 when slip vectors are estimated using an automatic method for numerous samples on faults because such slip vectors might be inaccurate for some samples. Large errors in slip vectors will yield large errors in the unfaulting shifts computed using method 2, because the unfaulting equations with slip vectors serve as hard constraints for this method. For slip vectors with errors, method 1 is preferred because it computes a least-squares solution of the unfaulting equations, which can be weighted according to some measure of the quality of estimated slips.

If instead fault slip vectors are manually interpreted for only a limited number of samples alongside faults, then we suggest method 2. For this method, the unfaulting equations constructed from the interpreted slip vectors serve as hard constraints for computing unfaulting shifts; therefore, the resulting unfaulted image is guaranteed to be consistent with the interpretation.

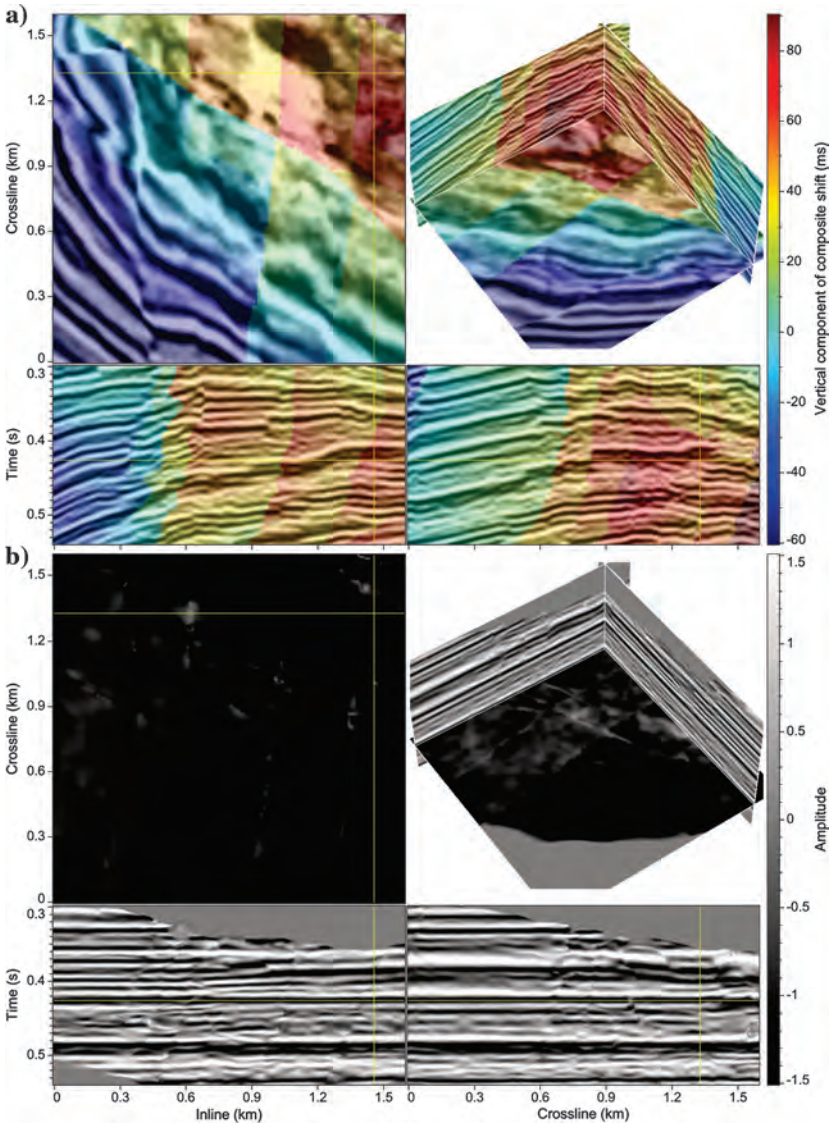

Figure 11. (a) Composite shifts are computed and then used to obtain (b) an unfaulted and unfolded image.

APPLICATION

The synthetic examples shown in Figure 8 demonstrate that both methods work well in unfaulting normal, reverse, and intersecting faults. As an additional test, method 1 was further applied to a real seismic image complicated by intersecting faults.

From the 3D seismic image shown in Figure 9a, we first used the methods described by Wu and Hale (2015a) to compute fault surfaces and dip slip vectors. Fault throws, the vertical components of dip slips, are displayed in color in Figure 9a. Note that fault throws are nonnegative, which indicates that the faults shown here are normal faults. We observe that most fault surfaces intersect others, and from the horizontal slice in Figure 9a, the strike angles for the intersecting faults differ by approximately 60°.

Using the computed fault surfaces and slip vectors, we then computed unfaulting vector shifts $\mathbf{r}(\mathbf{w})$ in unfaulted space using method 1. The vertical components of the shifts are displayed in Figure 9b. The inline and crossline components of the shifts are not shown. The intersections of faults are apparent in the horizontal slice of the vertical shifts shown in Figure 9b.

Using the unfaulting vector shifts $\mathbf{r}(\mathbf{w})$, we then compute the unfaulting mapping $\mathbf{x}(\mathbf{w}) = \mathbf{w} + \mathbf{r}(\mathbf{w})$, which undoes the faulting in the seismic image (Figure 10a) to produce the unfaulted image shown in Figure 10b. In this unfaulted image, seismic reflectors in all image slices are more continu-

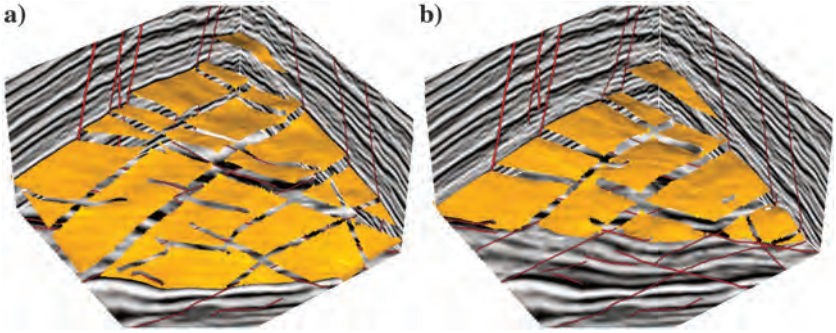

Figure 12. Two horizon surfaces (colored by yellow depth) are extracted using composite shift vectors that map an image from input space to unfaulted and unfolded space. The vertical component of the composite shift vectors is displayed in Figure 11a.

ous across faults than those in the original image slices shown in Figure 10a. For the fault with large slips highlighted by the red arrow in Figure 10a, footwall and hanging-wall sides are moved significantly to align the reflectors on opposite sides of the fault, as shown in Figure 10b.

For an unfaulted image with seismic reflectors that are continuous across faults, seismic horizon interpretation is more straightforward, for either manual or automatic methods. Here, we used the method described by Luo and Hale (2013) to compute vector shifts that undo the folding in the unfaulted image (Figure 10b), to obtain the unfolded image shown in Figure 11b. In the slices of the unfolded image shown in Figure 11b, the seismic reflectors are horizontal. As discussed by Luo and Hale (2013), using the unfolding vector shifts together with unfaulting vector shifts, we can compute composite vector shifts, which enable us to directly map the input seismic image to the unfaulted and unfolded space. The vertical components of the computed composite vector shifts are displayed in Figure 11a.

Using the composite vector shifts, we are able to extract any number of seismic horizons from the input seismic image in the input space, as discussed by Luo and Hale (2013). Figure 12 shows two seismic horizons extracted using the computed vector shifts. Our unfaulting processing facilitates the extraction of such complicated horizon surfaces by aligning seismic reflector across faults.

CONCLUSION

We have described two methods to automatically undo faulting in 3D seismic images. Both methods require precomputed fault positions and slip vectors at faults. Both methods efficiently compute vector shifts that simultaneously move fault blocks and faults themselves to undo faulting in seismic images. The cost of the unfaulting methods mainly depends on the size of an input seismic image, but it does not depend on the number of faults. For the previous 3D real example with $120 \times 200 \times 200$ image samples, the total runtime was on the order of a few minutes on an eight-core workstation. The unfaulting methods are more efficient than the unfolding method, which also costs a few minutes for the same example.

We suggest using method 1 when fault slips are estimated automatically for most samples at faults because this method computes a least-squares solution of the unfaulting equations constructed from estimated slips. Method 2 is preferable if fault slips are manually interpreted for only a limited number of samples at faults because this method considers the interpreted slips as hard constraints when computing unfaulting shifts.

One limitation of both methods is that they do not truly reverse the geologic deformation of faulting. We construct simple partial differential equations for samples away from faults in fault blocks to obtain smooth unfaulting shifts for these samples. The unfaulting shifts are allowed to vary more significantly in directions normal to seismic reflectors than in directions parallel to reflectors by using spatially variant tensor fields as coefficients in these partial differential equations. Although these simple equations can be solved efficiently and unfaulted images appear reasonable, it might be possible and preferable to use a more geologically and geomechanically correct way to compute unfaulting shifts for samples away from faults.

ACKNOWLEDGMENTS

This research is supported by the sponsors of the Consortium Project on Seismic Inverse Methods for Complex Structures. The real 3D seismic image used in this paper was graciously provided by K. Rutten and B. Howard, via TNO (Netherlands Organization for Applied Scientific Research). We appreciate suggestions by V. Aarre and two anonymous reviewers that led to significant revision of this paper.

REFERENCES

Aurnhammer, M., and K. Tonnies, 2005, A genetic algorithm for automated horizon correlation across faults in seismic images: IEEE Transactions on Evolutionary Computation, **9**, 201–210, doi: 10.1109/TEVC.2004.841307.

Fehmers, G. C., and C. F. Höcker, 2003, Fast structural interpretation with structure oriented filtering: Geophysics, **68**, 1286–1293, doi: 10.1190/1.1598121.

Hale, D., 2013, Methods to compute fault images, extract fault surfaces, and estimate fault throws from 3D seismic images: Geophysics, **78**, no. 2, O33–O43, doi: 10.1190/geo2012-0331.1.

Liang, L., D. Hale, and M. Maučec, 2010, Estimating fault displacements in seismic images: 80th Annual International Meeting, SEG, Expanded Abstracts, 1357–1361.

Luo, S., and D. Hale, 2013, Unfaulting and unfolding 3D seismic images: Geophysics, **78**, no. 4, O45–O56, doi: 10.1190/geo2012-0350.1.

Rice, J. R., 1983, Constitutive relations for fault slip and earthquake instabilities: Pure and applied geophysics, **121**, 443–475, doi: 10.1007/BF02590151.

Van Vliet, L. J., and P. W. Verbeek, 1995, Estimators for orientation and anisotropy in digitized images, *in* J. van Katjweik, ed., Proceedings of the first annual conference of the Advanced School for Computing and Imaging: ASCI, 442–450.

Wei, K., 2009, 3D fast fault restoration, U.S. Patent 7,480,205.

Wei, K., and R. Maset, 2005, Fast faulting reversal — draft version 3: 75th Annual International Meeting, SEG, Expanded Abstracts, 771–774.

Wu, X., and D. Hale, 2015a, 3D seismic image processing for faults: 85th Annual International Meeting, SEG, Expanded Abstracts, 1728–1733.

Wu, X., and D. Hale, 2015b, Horizon volumes with interpreted constraints: Geophysics, **80**, no. 2, IM21–IM33, doi: 10.1190/geo2014-0212.1.